Optimum design and performance of a solar dish microturbine using real component characteristics

Giacomo Gavagnin[a], Sergio Rech[c], David Sánchez[a,*], Andrea Lazzaretto[b]

[a] *University of Seville, Camino de los descubrimientos s/n, 41092 Seville, Spain*
[b] *Department of Industrial Engineering - University of Padova, via Venezia 1, 35131,Padova, Italy*
[c] *Interdepartmental Center "Giorgio Levi Cases" for Energy Economics and Technology - University of Padova, via Marzolo 9, 35131 Padova, Italy*

Abstract

The conversion of solar energy into electricity is a fundamental step in the transition to a renewable electric scenario. Concentrated solar systems may have a crucial role in this transition, both for large scale solar-only or hybrid systems and small scale, distributed applications. In the latter case, micro gas turbines are simple and versatile systems which can generate electricity with a fairly high efficiency compared to other systems of similar output.

The aim of the paper is to find the optimum design and performance of microturbines powered by parabolic dish collectors using an innovative methodology which integrates the design and off-design models of the total system. Thus, in contrast to the common practice of assigning an estimated efficiency to each component of the engine, the procedure hereinafter evaluates draft geometries and efficiencies of these components at the same time, according to the corresponding inlet/oulet thermodynamic states. This reduces the number of iterations that is required to finalize the design process.

A sensitivity analysis is performed to search the pressure ratio that maximizes solar-to-electricity efficiency at constant air mass flow rate and turbine inlet temperature and for a given location. Maximum values in the range from 18.0% to 21.7% are obtained for a pressure ratio of 3.2 when turbine inlet temperature changes between 800 °C (*base-case* system) and 900 °C and direct solar irradiance (DNI) is 800 W/m^2.

*Corresponding author
Email address: ds@us.es (David Sánchez)

The methodology allows also to simulate the performance of the system when different design DNI's are considered with the aim to maximize the annual yield of the system (maximum average efficiency rather than maximum design point efficiency). Simulations performed for Beijing, Seville and San Diego showed that quite different design DNI's (610 to 815 W/m^2) are to be chosen ir order to get the maximum annual (average) efficiency: 11% to 16% for the base-case system and 14% to 19% for a more advanced design.

Keywords: Microturbine, Solar dish, Volumetric cavity receiver, Design and off-design

1. Introduction

Solar power is the most abundant and distributed primary energy source on Earth. In the last decades, academic and governmental organizations have attempted to develop power systems able to collect and convert this energy into electricity. Many of these efforts were aimed at demonstrating the technical and economic feasibility of systems that integrate solar energy collection and concentration devices with well established power generation systems. Among these conventional technologies, the focus has always been on the utilization of gas turbines for their small footprint and low capital cost [1–5].

One of the most recent attempts to develop small scale solar power generators based on micro gas turbine technology is the OMSoP project (*Optimised Microturbine Solar Power Generator*), funded by the European Commission within the 7^{th} Framework Programme [6]. The OMSoP consortium has already published many works related to this type of systems [7–12]. Giovannelli [7, 8] presents a review of the current state of the art in the area of small-scale concentrated solar thermal power systems based on dish collectors. Lanchi et al. [9] present the experimental solar unit developed by ENEA (Italian National Agency for New Technologies, Energy and Suitable Economic Development) for the OMSoP project. Cerri et al. [10] propose the integration of solar dishes with advanced semi-closed cycles micro-turbines. Sanchez et al. [11] analyze the potential of selected markets for the wolwide

commercial deployment of OMSoP systems. Gavagnin et al. evaluate the manufacturing, transportation and installation costs of the simple recuperated solar-only and hybrid systems in [12] and the economic and financial appraisal of the project for simple recuperated and intercooled and intercooled/reheated advanced layouts in [13].

Micro gas turbines (mGT) have a power output in the range from a few kilowatts [14] to half a megawatt [15], even if this upper limit might change between 250 kW and 1 MW depending on the source. They typically include single stage radial turbomachinery with moderate pressure ratio (though higher pressure ratios in combination with axial flow machinery in larger engines) and an internal heat recovery device (compact heat exchanger [14]) to enhance efficiency. These components are typically arranged in a single shaft configuration although multiple-shaft layouts have also been considered [16].

Solar micro turbines typically make use of a parabolic dish to collect and concentrate solar energy onto a receiver which in turn converts it into heat. The concentration ratio of these collectors is very high, therefore enabling the very high temperatures that are needed for the engine to attain high efficiency [17]. With the aforecited OMSoP project, the Royal Institute of Technology in Stockholm (KTH) tested two different solar receiver prototypes: a cavity volumetric pressurized receiver with foam absorber [18, 19] and an impingement cavity receiver [20]. Aichmayer et al. studied the integration of volumetric receivers in several applications such as solar systems for off-grid energy production [21] and polygeneration in rural areas [22], either in simple or combined cycle configuration [23], whilst Wang et al. [24] studied the integrated dish-mGT design using solar systems with impingement receivers. These activities add to the past work with these systems for space, military and civil power applications: Kesseli et al. calculated the performance of a micro turbine engine composed by stock turbocharger components in [25] while Dickey [26] presents the experimental performance of a Capstone micro turbine integrated with a field of heliostats. More recently, LeRoux and Meyer make use of a lumped-volume approach to simulate the performance of a small-scale dish-mTG system using data from standard off-the-shelf Garrett turbocharger technology and a model of open-cavity tubular receivers [27]. Semprini et al. also employ models of solar-only and hybrid mGT systems based on lumped-volumes and efficiency maps of turbomachinery taken from literature [28].

In contrast to these past works, the current paper presents an integrated

procedure to design a solar mGT system and to evaluate its annual performance. The objective is twofold: 1) to find the optimum design of the mGT and its components for a specified design-point DNI, 2) to find the best design of the solar subsystem in various locations by identifying the design-point DNI that yield maximum annual (average) solar-to-electric efficiency.

The first objective is accomplished by building detailed design models of the mGT turbomachinery with the capacity to produce a geometry for maximum efficiency. In so doing, turbomachinery efficiencies are not taken from literature (as it is usually the case) but rather it is evaluated for the particular geometry that best fits the real inlet/outlet thermodynamic states. These design models of the compressor and turbine are also used to calculate their corresponding performance maps (speed lines and efficiency islands) which are later used to predict their behavior at partial load.

The second goal is achieved by building detailed off-design models of the dish-mGT systems based on the performance maps of the individual components and on a particular control strategy that ensures highest efficiency and avoids overheating or overspeeding of the components. The optimum design of the solar subsystem in various locations can thus be obtained by simulating the complete dish-mGT system over a year at different design values of the Direct Normal Irradiance. All the steps of this integrated design and off-design analysis, which have not been found elsewhere in literature, are presented in the paper.

2. Dish-mGT integrated solar systems

Dish-mGT integrated solar power generator systems are mostly based on the simple recuperated Joule-Brayton cycle, Fig. 1, though other configurations including intercooling and reheat have been proposed in literature [13].

The parabolic dish is responsible for the heat supply. This is a well established technology with many different designs having been tested mostly for integration in dish-Stirling systems, [29–31]. Nevertheless, there is also experience in the integration of parabollic dish collectors and micro turbines. A complete dish-mGT assembly based on solarized turbocharger-derived engines was studied in the mid 1980s by NASA (National Aeronautics and Space Administration) through the *Brayton Power System* and *Solar Advanced Gas Turbine Engine* projects [32, 33]. Amsbeck et al. reported the testing of a solar-hybrid mGT at the Plataforma Solar de Almeria [34] and

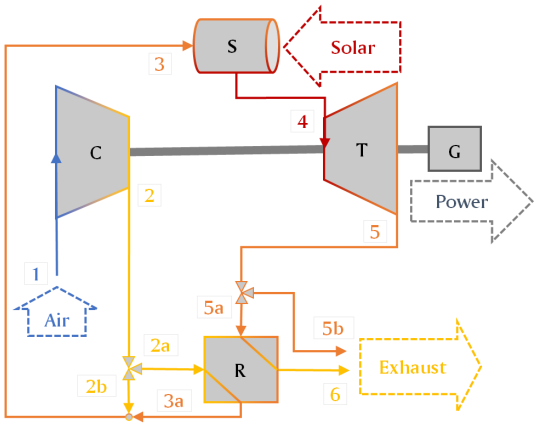

Figure 1: Single-shaft recuperative microturbine with integrated solar receiver.

Dickey et al. published test results of an adapted Capstone mGT operated on solar energy at the Weizmann Institute [35]. Finally, Kesseli et al. reported tests carried out by Brayton Energy with a system including dish collectors, micro gas turbines and a compressed air storage system [36]. In these systems, solar volumetric receivers is often used because of the higher efficiency as compared to cavity receivers in either tubular or impingement configuration [37, 38]. This experience in the integration of the prime mover and the collector is complemented by the numerous studies in literature where the differences between using adapted turbochargers or small gas turbines designed from scratch are discussed [39–44].

In the recuperated Joule-Brayton cycle shown in Fig. 1, the available heat carried by the gases leaving the expander is used to preheat the air delivered by the compressor before this enters the combustor, with the aim to increase the thermal efficiency of the engine. This layout is best exploited when associated to low pressure ratios which enable the utilization of single-stage radial turbomachinery coupled to a solar receiver which as a mere substitute for the combustor of a conventional mGT [16]. The flow diagram is as follows. Ambient air that enters the compressor (C) where it is pressurized (1-2). This air stream then flows into the cold side of the counter-flow compact recuperator (R) where it is heated by the hot exhaust air flowing out from the turbine (2a-3a). Once preheated, the air enters the solar receiver (S) where it is heated up further by the solar energy collected by the parablic dish and concentrated onto the focal point where the solar receiver is mounted. This

component is a volumetric, pressurized receiver with a SiC foam absorber and a quartz glass window that lets solar energy in whilst reducing both pressure and convective heat loses. Hence, the concentrated solar beams entering the receiver heat the foam absorber which, in turn, raises the temperature of air flowing through it (air acts as a coolant for the absorber). The air exiting the receiver flows into the turbine (T) where it is expanded (4-5) and it is then sent to the hot end of the recuperator where it is cooled down by the compressor delivery air before being released to the atmosphere (5a-6). When the available solar radiation exceeds a maximum value (upper threshold), a fraction of the total mass flow rate through the engine bypasses both sides of the recuperator, thus reducing the inlet tempeature to the solar receiver (3) and avoiding overheating of the system.

The electric generator (G) is mounted on the same shaft of the turbine and compressor, hence rotating at a very high and variable speed (in the range 100-150 krpm). This means that power electronics are required to ensure that the voltage and frequency of the electric output are stable and in compliance with the requirements of the grid.

3. Methodology

The methodology used to find the optimum design and performance of the solar-mGT system is based on an integrated procedure which links the design and off-design models of the system. Both models are solved with a modular-sequential approach which relies on the conservation of mass, momentum and energy and on certain correlations to characterize pressure and energy losses. The library Coolprop® [45] is used to compute the equation of state and to obtain the thermodynamic properties of air, considered to be dry real gas. The models have been implemented in the commercial software Matlab® on the assumption that all the processes take place in equilibrium [46].

The first stage of the design module is to calculate the thermodynamic cycle, the components and system efficiencies (except for the regenerator, whose target effectiveness is set by the user) and the basic geometries of the main components at nominal conditions. To this end, both one dimensional (1-D) and zero dimensional (0-D) approaches are used: radial turbomachinery (1-D), solar receiver (0-D), recuperator (0-D) and solar dish (0-D). The design space is limited by a sufficiently large range of pressure ratios (2.5-4, see Section 4.1) where potential designs are explored in order to attain highest solar-to-electric efficiency at the design point. The basic geometry of the

turbomachines, which includes the meridional passage and blades, is used to produce their corresponding performance maps (i.e., specific energy change and isentropic efficiency versus corrected mass flow rate), which are then used by the off-design model (see Fig. 8) to evaluate the behavior of the system when subjected to boundary conditions different from the design ones. This off-design model relies on a suitable control strategy which ensures the safe operation of the system within a certain range of boundary conditions.

3.1. Design model

The structure of the design model is shown in the flowchart in Fig. 2 whose input data are lised in Table 1. A *base-case* system and an *advanced* system are considered with the same structure of the solver, corresponding to two different sets of Turbine Inlet Temperature (TIT) and recuperator effectiveness ($\varepsilon_{rec,DP}$): 800°C-85% and 900°C-90%, respectively.

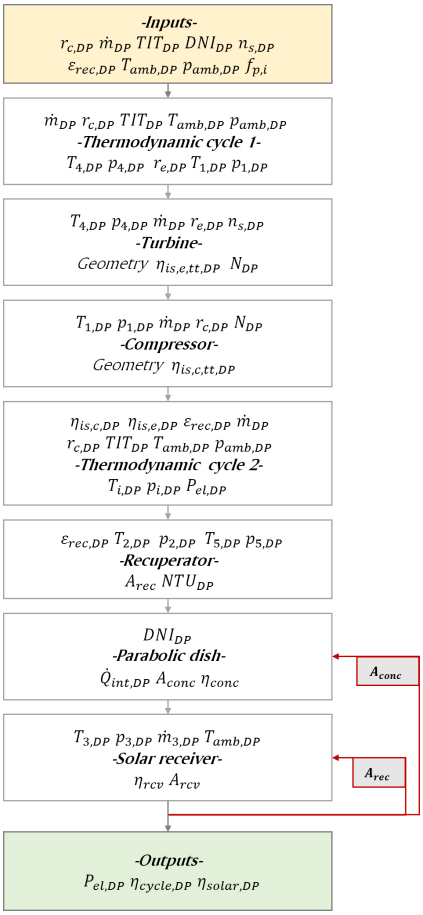

Figure 2: Design model flowchart.

Main system specifications			
DNI_{DP}	800 W/m^2	(sensitivity 400 W/m^2-1000 W/m^2)	
$r_{c,DP}$	3	(sensitivity 2.5-4)	
$\dot{m}_{air,DP}$	0.1 kg/s		
TIT_{DP}	800 °C ($base$) 900 °C ($adv.$)	$\varepsilon_{rec,DP}$	85 % ($base$) 90 % ($adv.$)
$T_{amb,DP}$	25 °C	$p_{amb,DP}$	101325 Pa
$f_{p,rec,c,DP}$	97.0 %	$f_{p,rec,h,DP}$	98.5 %
$f_{p,rcv,DP}$	96.0 %	$f_{p,in/out,DP}$	99.5 %
$\eta_{mech,DP}$	99.0 %	$\eta_{el,DP}$	90.0 %
$\Delta T_{turb,DP}$	5 °C	$n_{s,turb,DP}$	0.55

Table 1: Set of the independent variables (inpu parameters).

The thermodynamic (working) cycle of the engine is calculated from the information in Table 1 as shown in Fig. 2. Then, block *"Thermody-*

namic cycle 1" calculates the inlet conditions (pressure and temperature) to each turbomachinery along with the corresponding turbine expansion ratio ($r_{e,DP} = \frac{p_4}{p_5}$) for a given pressure ratio of the compressor($r_{c,DP} = \frac{p_2}{p_1}$). In these calculations, pressure losses across solar receiver, recuperator and inlet/outlet ducts are taken into account by means of the pressure loss factors ($f_p = \frac{p_{out}}{p_{in}}$) in Table 1. With this information, the turbomachinery 1-D design models (blocks *"Turbine"* and *"Compressor"*) calculate the draft geometries of turbine and compressor and hence their isentropic efficiencies and rotational speed. These data are the used to complete the simulation of the thermodynamic cycle by calculating the outlet states of each turbomachinery and the complete heat balance of the recuperator. Once the thermodynamic cycle is calculated fully, the recuperator can be designed using the $\varepsilon - NTU$ approach to calculate the Number of Transfer Units (NTU) and, in turn, the total heat transfer area of the selected counter-flow configuration that yields the target effectiveness specified originally.

The tools to design the solar subsystem include the parabolic dish and receiver design models. The sizes of these components aperture area of the collector and window area of the receiver are optimized for the nominal conditions obtained by the design model of the mGT through minimization of heat losses. Inputs to the parabolic dish model are the nominal DNI and the heat input to the receiver with which the receiver model then calculates the air outlet temperature (TIT). Two iterative loops are finally used to optimize the aperture area of collector and receiver:

1. The inner loop searches for the optimum size of the receiver window which stems from a balance between heat input from the collector and heat losses tot he environment.
2. The outer loop corrects the dish aperture area until the receiver outlet temperature is equal to the specified TIT at the rated conditions.

3.1.1. Thermodynamic cycle

The blocks calculating the design thermodynamic cycle in Fig. 2 ("Thermodynamic cycle 1 and 2") include mass and energy conservation and component efficiencies [47]. Thus, the outlet conditions from compressor and expander are calculated from the total-to-total pressure ratios and the isentropic efficiencies whilst the inlet and outlet states of the recuperator are computed from a fixed effectiveness and pressure loss factors ($\varepsilon_{reg,DP}$, $f_{p,reg,C,DP}$ and $f_{p,reg,H,DP}$ in Table 1). With this information, the model calculates all

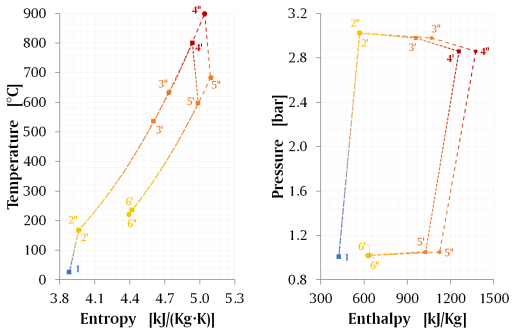

Figure 3: Temperature-entropy (left) and pressure-enthalpy (right) diagrams of the *base-case* and *advanced* systems.

the thermodynamic states in Fig. 1 along with the mechanical shaft output for a specified mass flow rate at compressor inlet ($\dot{m}_1$=0.1 kg/s). The net electric power output is then calculated by applying the electric and mechanical efficiencies. Figure 3 shows the thermodynamic cycles of both the *base-case* and *advanced* systems.

3.1.2. Turbomachinery

The design models of compressor and turbine are based on the one-dimensional approaches proposed by Aungier in [48] and [49] and provide the total-to-total isentropic efficiencies and the rotational speed of the sized stages [50]. In the main, this approach assumes constant flow field variables (velocity, temperature and pressure) at each cross-section of the flow passage (channel). These variables are obtained from steady-state mass, energy and momentum balance equations computed along the mean stream surface using empirical fluid dynamics and total pressure loss correlations. A boundary layer model is applied to take into account the total pressure loss due to skin friction between the fluid and passage walls, with the the resulting variation of Reynolds number along the mean stream surface being used to evaluate the entropy rise and, in turn, the isentropic efficiency.

The matching of compressor and turbine is initiated in the latter component, for which a reference specific speed $n_{s,t}$=0.55 is adopted based on recommendations by Rodgers [51] and Aungier [49], Eq. (1)). Based on this specification, the rotational speed that yields highest turbine efficiency, and thus cycle efficiency, is calculated (see also [52, 53]). With this information and the spouting velocity $C_{0,is}$ (velocity obtained in a total-to-static

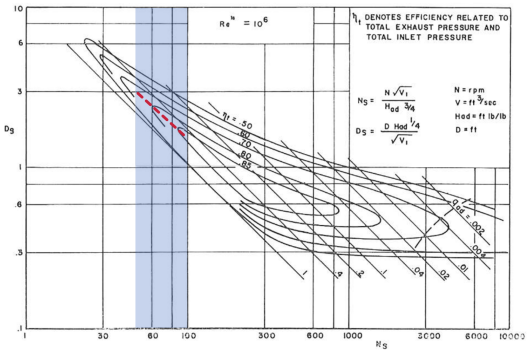

Figure 4: Specific speed vs. specific diameter compressor showing the *Cordier* line for radial stages in dashed red. Adapted from [54]

isentropic expansion), the tangential speed of the blade ($U_{tip,t}$) and the corresponding rotor diameter ($d_{tip,t}$) can be calculated, Eq. (2)) provided by Aungier [49].

$$\omega_{DP} = n_{s,t} \frac{\Delta h_{is,tt,t}^{0.75}}{\dot{V}_{0,t}^{0.5}} \tag{1}$$

$$\nu_{ts,t} = 0.737 \cdot n_{s,t}^{0.2} = \frac{U_{tip}}{C_{0,is}} \tag{2}$$

The rotational speed of the compressor is the same as that of the expander and it can be used to calculate the specific speed ($n_{s,c}$) and diameter ($d_{s,c}$) of the machine, Eq. (3,4). This information is obtained by interpolating the corresponding n_s vs. d_s chart for maximum compressor efficiency (also *Cordier* line, sohwn dashed red in Fig. 4) in the range of application of radial turbomachinery ($50<n_{s,c}<100$) [54]. The specific diameter ($d_{s,c}$) so obtained is used to calculate the tip diameter of the compressor impeller ($d_{tip,c}$).

$$n_{s,c} = \omega_{DP} \frac{\dot{V}_{0,c}^{0.5}}{\Delta h_{is,tt,c}^{0.75}} \tag{3}$$

$$d_{s,c} = 2.865 \cdot n_{s,c}^{-0.946} = d_{tip} \frac{\Delta h_{is,tt,c}^{0.25}}{\dot{V}_{0,c}^{0.5}} \tag{4}$$

The sizing of the turbine is performed in the following order: rotor, nozzle, inlet volute and exhaust diffuser. For these elements, a draft geometry is produced from a set of default design specifications in combination with

empirical correlations based on the reference specific speed, as suggested by Aungier [49]. These specifications include the spouting velocity of the stage, specific diameter of the rotor, inlet flow angle, number, chord and thickness of the blades and inlet-to-outlet radii ratio of the nozzle. The main design steps applied to these data are summarized below, as described in [49] where more details can be found:

- The main geometrical parameters of the rotor are calculated from $n_{s,t}$ and $d_{tip,t}$ under the assumption that inlet velocity is radial (relative rotor inlet angle is 90°). The meridional plane of the compressor is sized so as to minimize the variation of area between the inlet and outlet sections under the constant mass flow rate restriction, Fig. 5. The number, mean line gometry and thickness distribution of the blades is then calculated with empirical correlations and the feasibility of the geometry so obtained is verified against the specific guidelines proposed by Aungier [49];

- In order to size the nozzle, the minimum number of blades needed to yield radial relative flow at the inlet to the wheel and, at the same time, a blade loading lower than 1 is calculated;

- An elliptical configuration is considered for the volute, where the variation of cross sectional area comes determined by mass conservation, a constant size parameter $SP = \frac{\sqrt{\dot{V}_{out}}}{\Delta H_{is}^{0.25}}$=1 equal to 1 and the continuity of the angular momentum at the nozzle row inlet;

- The exhaust diffuser design is obtained from empirical correlations on the assumptions that the ratio between outlet and inlet areas is equal to 1.5 and the divergence angle is 11°.

The aforedescribed procedure generates a draft geometry for the actual design point, yielding a certain mass flow rate and total-to-total expansion ratio. These values are then used to correct the design until the target values are attained. Once the final design is obtained, the corresponding performance map is produced by merely calculating the performance of the expander for different sets of boundary conditions, including those specific conditions for which sections of the machine get choked.

The compressor design process is different to the turbine as it does not start from a set of sepcifications but, on the contrary, it is carried out directly

by means of the empirical performance model proposed by Aungier [48]. In this, guessed values of the total-to-total isentropic efficiency and total pressure loss coefficient (from rotor inlet to volute outlet) are initially assumed and the geometry of the compressor components are evaluated as follows:

- The impeller inlet section is sized in order to minimize the relative Mach number at the shroud, whilst the outlet diameter is influenced by the blade exit angle as a result from a trade-off between stage work and the distortion and slip factors for each d_{tipc} (see Eqs. (3) and (4)), Fig. 5. The number of blades results from the minimum value yielding a blade loading not lower than 0.9;

- The diffuser can be of the vaned or vaneless type. In the former case, the number of vanes, the area ratio and the divergence angle result from an optimization process to yield maximum efficiency with a total load lower than 0.3;

- The outlet radius of the volute is calculated iteratively by fixing a size parameter of 1.05. The radius distribution is then obtained from continuity by keeping the size parameter constant.

The performance maps of compressor and turbine for the *base-case* and *advanced* systems are shown in Fig. 6 respectively. These maps show total-to-total isentropic enthalpy change and isentropic efficiency versus mass flow rate for shaft speeds ranging from 70% to 115% of the design point value.

The performance of small turbomachinery is strongly affected by the clearance between the rotor and the shroud (casing), [55]. Experimental results obtained by Rodgers et al. show that turbine efficiency increases as the clearance is reduced whilst compressor efficiency increases for increasing clearance up to a maximum value from which it starts to decline [56]. Head et al. [55] demonstrate that the effect of this gap is neither constant nor proportional to the scale as observed in the following equation used to design the clearance in turbine and compressor δ_{cl}:

$$\delta_{cl} = \delta_{cl,ref} \cdot \left(\frac{b_{blade}}{b_{blade,ref}} \right)^{0.6}, \tag{5}$$

Equation 5 is referred to a reference blade height ($b_{blade,ref} = 5$ mm) with a reference clearance gap ($\delta_{cl,ref}$ is 0.4 mm and 0.3 mm for turbines and

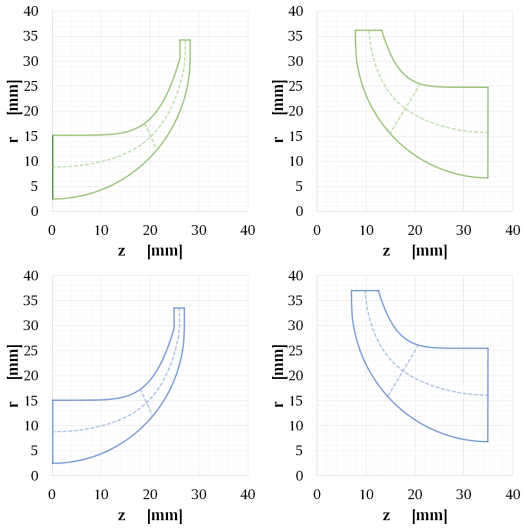

Figure 5: Meridional flow passage of the compressor impeller (left) and turbine wheel (right) for the *base-case* (above) and *advanced* (below) systems.

compressors, respectively). Typical absolute and relative (ratio of clearance gap and blade height) clearance versus blade height trends are shown in Fig. 7, evidencing that the relative gap decreases for increasing blade height in spite of a the higher absolute clearance clearance. The effect of roughness is accounted for with a classical skin friction model based on boundary layer analysis where a peak-to-valley roughness of 1 µm is assumed [57].

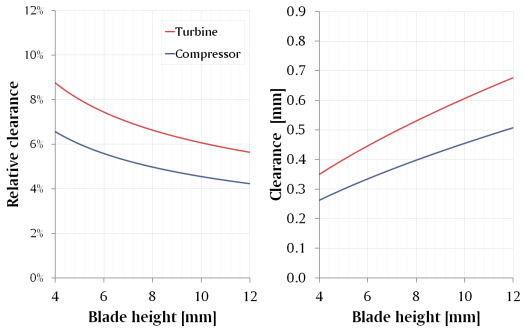

Figure 7: Relative (left) and absolute clearance (right) gaps vs. blade height distributions.

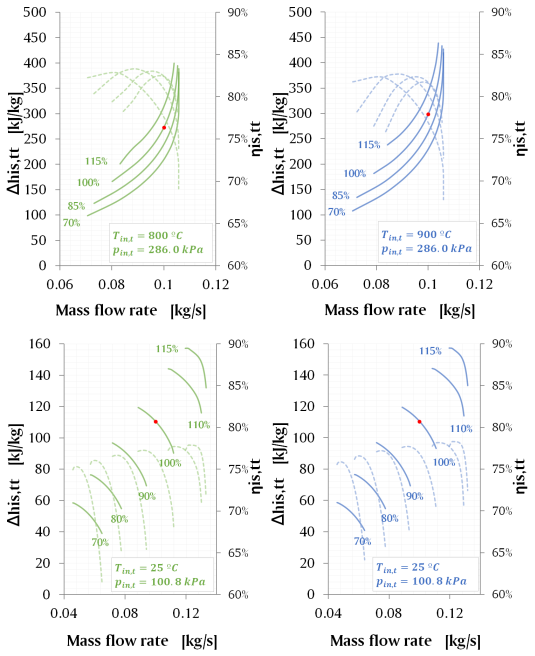

Figure 6: Turbine (above) and compressor (below) maps for the *base-case* (left) and *advanced* (right) systems: total-to-total isentropic enthalpy drop vs. mass flow rate (solid) and total-to-total isentropic efficiency vs mass flow rate (dashed).

3.1.3. Recuperator

The design model of the regenerator is based on the well-know $\varepsilon - NTU$ approach [58] which is fed with the inlet and outlet conditions at design point calculated with blocks "thermodynamic cycle 1 and 2" in Fig. 2. The global heat transfer coefficient at design point is initially set to a constant value of $U_{r,DP} = 100$ W/(m^2·K. Then, the hot and cold heat capacities ($\dot{C}_{DP} = \dot{m}_{DP} \cdot \bar{c}_{p,DP}$) and heat capacity ratio ($r_{r,DP} = \dot{C}_{min,DP}/\dot{C}_{max,DP}$ are caculated, yielding the number of transfer units NTU_{DP} and the total heat transfer area $A_{ex,r}$ at design point. More considerations about how this method can be applied to recuperators in micro gas turbines can be found in [59–62].

$$NTU_{DP} = \frac{\log_e \frac{1-\varepsilon_{rec,DP}}{1-r_{rec,DP}\cdot\varepsilon_{rec,DP}}}{\dot{m}_{in,DP} \cdot \Delta h_{rec,DP}} \tag{6}$$

$$A_{ex,rec} = \frac{\dot{m}_{in,DP} \cdot c_{p,in,DP} \cdot NTU_{DP}}{U_{rec,DP}} \tag{7}$$

3.1.4. Cavity volumetric receiver

The simple model of the cavity volumetric receiver proposed by Aichmayer in [21] and modified by Semprini [28] to introduce the equations for grey bodies is used here, with optical properties evaluated at each specific wavelength. The model considers convective losses whereas the conductive loss and the utilization of a secondary concentrator are neglected.

The optical properties are taken from Roger [63]. They are wavelength-weighted values for a 5 mm thick fused silica glass window considering the solar radiation spectrum and the thermal radiation produced by a black body surface at 1100 °C. The radiation emitted by the glass window is calculated as that of a gray body at 600K (326.85°C) with emissivity and absorptivity equal to 0.8. The model includes the energy balance equations applied to the glass window, the cavity and the foam absorber as shown in Eqs.(**??**, with an additional equation for the absorber temperature, Eq.(15). The convective heat transfer coefficient on the outer wall of the window is based on a Nusselt number correlation for natural convection flow on inclined planes $h_{conv,DP} = f(\Theta_{incl})$ where the incliation angle is set to a constant value of $\Theta_{incl} = 60°$ [64]. With all this information, the outcome of the energy balance is expressed in terms of specific intercepted beam power ($I_{DP} = \dot{Q}_{int,DP}/A_{rec}$) and specific air mass flow rate per unit window area ($G_{DP} = \dot{m}_{3,DP}/A_{rec}$).

$$\dot{Q}_{rad,w} = I\alpha_{vis} + \sigma\left(\alpha_{th}T_{amb}^4 + \alpha_{infr}T_s^4 - 2\epsilon_{th}T_w^4\right) \tag{8}$$

$$\dot{Q}_{conv,w} = h_{conv}\left(T_w - T_{amb}\right) + U_w\left(T_w - T_3\right) \tag{9}$$

$$\dot{Q}_{rad,w} - \dot{Q}_{conv,w} = 0 \tag{10}$$

$$\dot{Q}_{rad,abs} = I + \sigma\left(\epsilon_{th} \cdot T_w^4 - T_{s,DP}^4 + \rho_{infr}T_s^4\right)\tau_{vis} \tag{11}$$

$$\dot{Q}_{conv,abs} = G\left(h_{cav} - h_4\right) \tag{12}$$

$$\dot{Q}_{conv,abs} - \dot{Q}_{rad,abs} = 0 \tag{13}$$

$$\dot{Q}_{conv,cav} = G\left(h_{cav} - h_3\right) - U_w\left(T_w - T_3\right) = 0 \tag{14}$$

$$T_{abs} = \frac{T_4 - T_{cav}}{2} \tag{15}$$

3.1.5. Parabolic dish collector

This Section describes the fundmentals of the collector model whose complete description can be found in [65, 66]. The concentrator geometry is a truncated portion of a paraboloid, the extent of which is defined by the rim angle Ψ_{rim}. This parameter can correlated to the ratio between aperture diameter d_{dish} and focal length f_{dish} as in Eq. (16) and its calue is set to $\Psi_{rim} = 45^{\circ}$ in this work. This choice is made to maximize the concentration ratio between the parabolic dish and the cavity receiver.

The amount of energy collected and concentrated by the collector on the receiver window is calculated considering a perfect parabola and then evaluating the deviations from this ideal collector due to reflection of non-parallel rays (sun shape error) and other reflection errors. The sunbeams are indeed not perfectly parallel due to finite angular size of the sun disc (about 9.6 mrad). The reflected rays form therefore an image of finite size centered on the focus, a so-called solar spot rather than an ideal single point image. In addition to this deviation from the ideal situation, there are other errors that come about during the manufacturing of the dish or because of the working conditions of the system. These errors are assumed to be random and are reported in the form of standard deviations units so that it is possible to determine their combined effect statistically. The total concentration error ($\sigma_{tot} = 6.7$ mrad) is considered constant and calculated as the cumulative effect of the sun shape effect, the slope error of the true parabolic shape, the non-specular reflection of the incident beam, the tracking error and the receiver alignment error. Table 2 shows the breakdown of the angular concentration errors considered for one standard distribution, i.e. when 68% of all measurements of the errors fall within the angular deviations noted.

In addition to the phenomena described above, the radiation emitted by the Sun is not evenly distributed across its disc and hence a standard distribution is assumed to handle this error as an additional contribution to the aforeslisted errors, according to Harris and Duff [67]. With all this information, the total irradiance (incoming concentrated radiation onto the receiver window can be calculated from the ideal description of a parabola

Concentration errors		
Type and source	Effective magnitude (1σ)	σ^2
Structure	5 mrad	25
Tracking sensor	2 mrad	4
Tracking drive non-uniformity	2 mrad	4
Receiver alignment	2 mrad	4
Total 1D	6.1 mrad	37
Mirror specular reflectance	0.5 mrad	0.25
Sun shape	2.8 mrad	7.84
Total 2D	2.8 mrad	8.09
Total	6.7 mrad	

Table 2: Sun image size, reflection, tracking and alignment errors.

reflecting parallel rays. To this aim, the dish is divided into finite rings for which the solar energy collected is calculated as in Eq.(20), where ρ_{dish} is the specular reflectance of the mirror surface and Γ_i is the fraction of heat flux captured calculated. This latter parameter is calculated as a function of the receiver window size as shown in Eq.(19). These calculations complement the total radiant flux reflected onto the focal point by a differential ring area of an ideal parabolic dish, as calculated in Eq. (18).

$$f_{dish} = \frac{d_{dish}}{4\tan\left(\frac{\Psi_{rim}}{2}\right)} \tag{16}$$

$$p_{dish} = \frac{2f_{dish}}{1+\cos\left(\Psi_{rim}\right)} \tag{17}$$

$$\left(\frac{d\Phi}{d\Psi}\right)_{i,DP} = \frac{8\pi \cdot DNI_{DP} \cdot f_{dish}^2 \cdot \sin\Psi_i}{\left(1+\cos\Psi_i\right)^2} \tag{18}$$

$$n_i = \frac{2}{\sigma_{tot}} \cdot \arctan\frac{d_{rec}\cdot\cos\Phi_i}{2p_{dish}}; \quad \Gamma_i = f\left(n_i\right) \tag{19}$$

$$\dot{Q}_{inter,DP} = \sum_{i=3^\circ}^{\Psi_{rim}} \rho_{dish}\cdot\Gamma_i\cdot\left(\frac{d\Phi}{d\Psi}\right)_{i,DP}\cdot\Delta\Psi_i \tag{20}$$

3.2. Off-design model

The off-design model is implemented in two steps:

1. Calculation of the overall/global performance maps showing the output and efficiency of the solar-mGT system as a function of DNI at a given ambient temperature.

2. Calculation of the annual yield (production of energy) for a given annual distribution of DNI and ambient temperature in a specified location.

The calculations in the first bullet point above are solved iteratively from the design point of the system (size of components, thermodynamic states of the cycle, performance maps of the compressor and turbine) as shown in the flowchart in Fig. (8). In summary, DNI and ambient temperature are varied independently in the range of interest to yield the off-design performance map of the system which provides the electric output produced in steady-state conditions for each pair (DNI,T_{amb}). Internally, the off-design submodel of each component is fed by the corresponding inlet state and boundary conditions and, in turn, calculates the outlet state that is used by the off-design submodel of the component downstream.

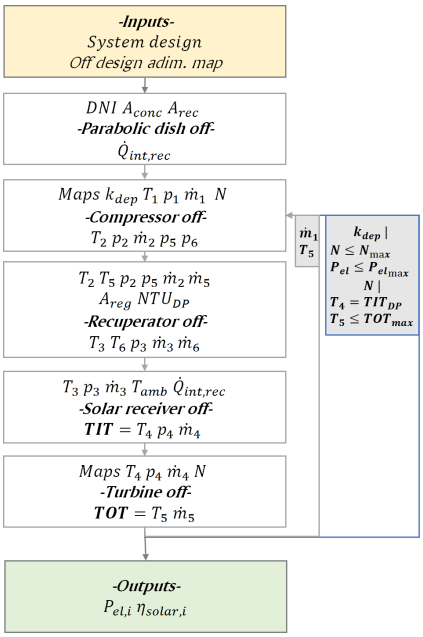

Figure 8: Flow chart of the off-design model.

The aforedescribed sequence of the solver must nevertheless be complemented by appropriate numerical and control strategies which ensures that the computation is stable and the operation of the system is safe under any set of boundary conditions. This numerical and control strategy is made up of two iterative loops that are needed to enable convergence of the solver.

The inner loop, shown grey in Fig. 8, exchanges information between the recuperator and expander and is used to calculate the turbine outlet temperature ($TOT = T_5$) and the air mass flow rate at equilibrium ($\dot{m}_1$). TOT is a required input to solve the regenerator submodel but, at the same time, it depends on the off-design performance of the expander downstream. At the same time, $\dot{m}_1$ depends on the pressure ratio and shaft speed of compressor and turbine, bringing in a cross-dependence between the operating point of both components. The inner loop starts off with guessed values of both variables (TOT,$\dot{m}_1$) and iterates through corrections until covergence is reached.

The outer iterative loop, blue line in Fig. 8, is used to implement the control strategy that maximizes the efficiency of the system and avoids operation in non-feasible conditions. The strategy is based on keeping turbine inlet temperature ($TIT = T_4$) at the rated value through variations of shaft speed (N). As expected, these changes in rotational speed bring about similar changes in both the enthalpy change and throughput across the compressor and expander. This strategy is valid for any set of boundary conditions as long as specific (upper) thresholds of the following critical variables are not exceeded: turbine outlet temperature (TOT), electric output (P_{el}) and shaft speed (N).

Indeed, a maximum TOT (TOT_{max}) is introduced to prevent overheating of the recuperator since this temperature is actually the inlet temperature to the hot end of the heat exchanger. Following the indications by McDonald [61], the limit is set to 675°C for the *base-case* (in which the recuperator is made up of 347 stainless steel) and to 750°C for the *advanced* system (in which super 347 stainless steel is used). It is worth noting that this limit can potentially be exceeded at DNI lower than the rated value only. In these conditions when $DNI < DNI_{DP}$, the air flow rate through the solar receiver ($\dot{m}_3 = \dot{m}_1$) is reduced through a reduction of shaft speed (N) in order to keep TIT at the rated value. This leads to a reduction in the engine's pressure ratio according to the performance maps of compressor and expander (see Fig. 6) and, in turn, TOT increases. Eventually, when the upper limit is reached the control strategy of shaft speed changes to keep TOT at the maximum value (Figs. 9 and 10).

Maximum values of shaft power P_{mech} and N are also in place to prevent overloading of the electric generator and overspeeding of the rotating components for $DNI > DNI_{DP}$. N_{max} is assumed to be equal to 115% of the rated value while $P_{mech,max}$ is calculated as a function of N (see Section

3.2.2). When $P_{mech,max}$ and/or N_{max} are reached, the recuperator is bypassed to a certain fraction (a similar fraction of the hot and cold flows are diverted to their corresponding outlets) as discussed in Section 2. This results in a reduction of the air temperature at the inlet (and most likely the outlet) of the solar receiver which implies a reduction in both P_{el} and N. A control parameter k_{dep} is introduced in the outer loop to evaluate the amount of air mass flow rate that is bypassed at the recuperator. It is defined as the ratio of mass flow rate that enters the recuperator to the the total mass flow rate at compressor outlet ($k_{dep} = \dot{m}_{2a}/\dot{m}_2$). It is also assumed that the system is shut down for $k_{dep} < 0.75$ and/or for $N/N_{DP} < 0.75$. A comparative study of the control strategies for pure solar microturbine systems, including recuperator by-pass, has recently been published by Ghavami et al. [68].

Figures 9 and 10 show the performance of the system when the afore-described control strategy is implemented, both for the *base-case* and *advanced* systems. The plots considered variable DNI and constant ambient temperature (25°C) even if similar plots for variable T_{amb} could have been produced. It is worth noting that that the limit TOT is reached only in the *advanced* system for DNI<420 W/m^2.

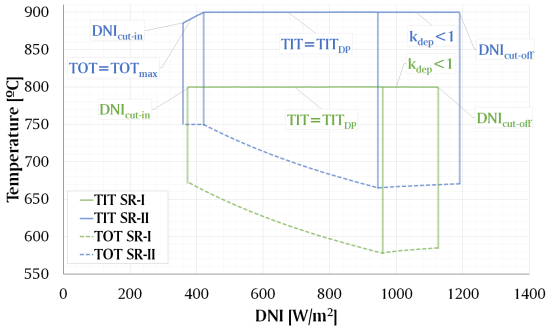

Figure 9: Off-design turbine inlet (TIT) and outlet (TOT) temperatures vs. DNI diagrams at rated ambient temperature ($T_{amb,DP}$) for the *base-case* (green) and *advanced* (blue) systems.

3.2.1. Turbomachinery

The off-design submodels of compressor and turbine calculate the isentropic and actual (polytropic) outlet states of these components, starting from the rotational speed and mass flow rate obtained from the performance

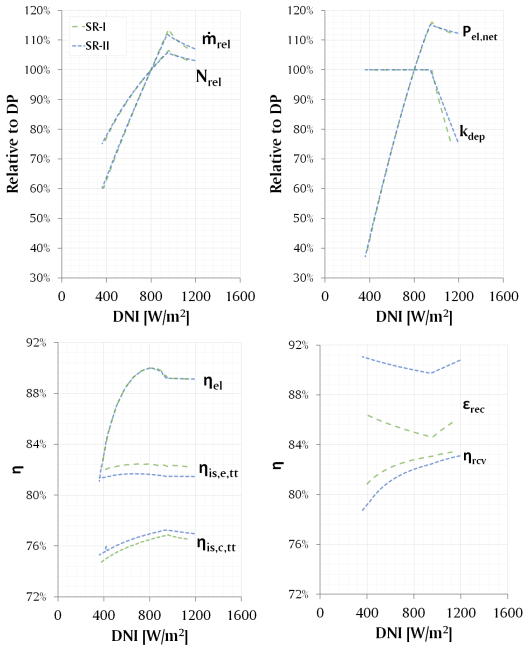

Figure 10: Main system control variables (above) and components efficiencies (below) vs DNI (at $T_{amb,DP}$).

maps obtained in the design phase (see Section 3.1.2). These maps are corrected to extend their validity to inlet temperatures and pressures different from the rated values that were used to calculate them. Similarity laws are also used to calculate the corrected inlet conditions as suggested in [69] and [70]. Compared to the typical formulas used to correct turbomachinery maps, that are valid for perfect gas, some factors accounting for real gas effects (variable specific heats and compressibility factor) are introduced. These similarity laws correlate the inlet mass flow rate and rotational speed to the isentropic enthalpy change and isentropic efficiency as in Eqs. (21-23) where δ is the ratio between the actual and reference inlet pressures ($\delta = p_{0,act}/p_{0,ref}$) and ϵ (Eq. (24)) and θ (Eq. (25)) take into account the changes in compressibility and specific heat ratio between the reference (ref) and actual ($real$) inlet conditions.

$$N_{eq} = \frac{N_{real}}{\sqrt{\theta}} \tag{21}$$

$$\dot{m}_{eq} = \frac{\dot{m}_{real} \cdot \sqrt{\theta}}{\delta} \cdot \epsilon \tag{22}$$

$$\Delta h_{is,eq} = \frac{\Delta h_{is,real}}{\sqrt{\theta}} \tag{23}$$

$$\epsilon = \frac{\gamma_{ref} \cdot \left(\frac{2}{\gamma_{ref}+1}\right)^{\frac{\gamma_{ref}}{\gamma_{ref}-1}}}{\gamma_{real} \cdot \left(\frac{2}{\gamma_{real}+1}\right)^{\frac{\gamma_{real}}{\gamma_{real}-1}}} \tag{24}$$

$$\theta = \left(\frac{V_{cr,real}}{V_{cr,ref}}\right)^2, \tag{25}$$

$V_{cr,real}$ and $V_{cr,ref}$ are calculated as in Eq.(25) where g_c is the gravitational acceleration, Z is the gas compressibility factor and R is the ideal gas constant:

$$V_{cr} = \sqrt{\frac{2 \cdot \gamma}{\gamma + 1} \cdot g_c \cdot Z \cdot R \cdot T_{in}}. \tag{26}$$

3.2.2. Electric generator

The off-design behavior of the electric generator is simulated using the empirical model developed by ENEA for the OMSoP project [8]. In this model, the mechanical-to-electric efficiency (η_{el}) depends on shaft work (P_{mech}), whose value is limited to prevent an excess of current intensity in the rotor, and rotational speed (N). Figure 12 shows the non dimensional relationships of the model.

3.2.3. Other components

The performance of the parabolic dish colector in off-design conditions does not differ from the design point due ot eh two degrees of freedom of the tracking system, which ensures that the dish is aligned with the sun. The off-design models of recuperator and solar receiver include the same equations as the design models but they are solved downstream rather than upstream. The variations of the global heat transfer coefficient with the mass flow rate are evaluated using Eq. (27).

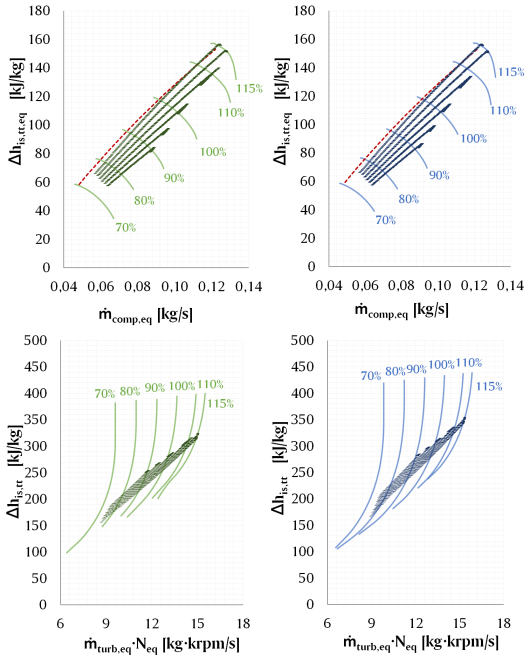

Figure 11: Corrected performnce maps used for the off-design model and off-design equilibrium points of compressor (above) and turbine (below) for the *base-case* (left) and *advanced* (right) systems.

$$U = U_{DP} \cdot \left(\frac{\dot{m}}{\dot{m}_{DP}} \right)^{0.8} \tag{27}$$

The pressure losses of recuperator, solar receiver and inlet/outlet ducts are varied according to Eq. 28.

$$\Delta p = \Delta p_{DP} \cdot \left(\frac{\dot{m}}{\dot{m}_{DP}} \right)^{1.21} \cdot \frac{\rho_{DP}}{\rho} \tag{28}$$

4. Results

This last Section presents three differents sets of results:

1. The results obtained by running the design model for the *base-case* ($TIT = 800°C$ and $\epsilon_{reg,DP} = 0.85$) and *advanced* ($TIT = 900°C$ and $\epsilon_{reg,DP} = 0.90$) systems for a design DNI of 800 W/m^2 and an air flow

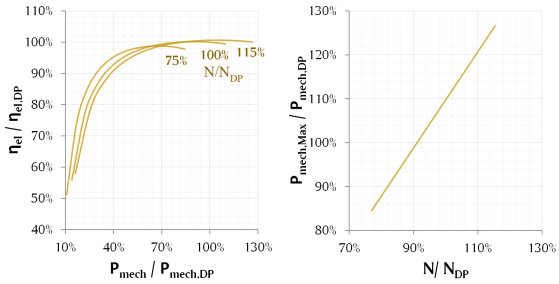

Figure 12: Electric generator efficiency vs. shaft work and rotational speed (left) and maximum shaft poewr vs rotational speed (right). Scales are non dimensional.

rate of 0.1 kg/s (see Table 1). In this analysis, the sensitivity to the rated pressure ratio is also assessed.

2. The off-design performance maps and the results of the annual simulation of the two systems mentioned in the previous bullet point;
3. The results of a sensitivity analysis with respect to the design DNI for three different locations (Beijing, Sivelle and San Diego).

4.1. Results at design point

The following performance metrics are used to characterize the aforecited systems:

- The solar-to-electric efficiency (η_{solar}) is defined as the ratio from net electric output (P_{el}) to total heat input to the system ($DNI \cdot A_{a,dish}$), Eq. (29). It can be applied to either design or off-design conditions.
- The specific output can be referred to the air mass flow rate ($\hat{P}_{el}$, Eq. (30)) or the aperture area of the parabolic dish ($\hat{P}_{solar,DP}$, Eq. (31)). It can be applied to either design or off-design conditions.
- The parabolic dish ($\eta_{dish,DP}$), solar receiver ($\eta_{rec,DP}$) and mGT cycle ($\eta_{cycle,DP}$) efficiencies, which are defined by Eqs. (32-34)

$$\eta_{solar} = \frac{P_{el}}{DN \cdot A_{a,dish}} \tag{29}$$

$$\hat{P}_{el} = \frac{P_{el}}{\dot{m}_1} \tag{30}$$

$$\hat{P}_{solar} = \frac{P_{el}}{A_{a,dish}} \tag{31}$$

$$\eta_{dish} = \frac{\dot{Q}_{int,DP}}{DNI_{DP} \cdot A_{a,dish}} \tag{32}$$

$$\eta_{rec,DP} = \frac{\dot{Q}_{mgt,DP}}{\dot{Q}_{int,DP}} \tag{33}$$

$$\eta_{cycle,DP} = \frac{P_{el,DP}}{\dot{Q}_{mgt,DP}} \tag{34}$$

A complete sensitivity analysis of system and component performance against pressure ratio ($r_{c,DP}$) is shown in Fig. 13 for the *base-case* and *advanced* systems (green and blue lines respectively). There are some interesting features to be noted. Firstly, it worth noting that even if a higher optimum (maximum η_{solar}) pressure ratio would have been expected for the *advanced* case, both systems find the optimum pressure ratio around 3.2. This is mostly because of the higher recuperator effectiveness ($\epsilon_{reg,DP}$ of the *advanced* case which promotes a lower pressure ratio to exploit the recuperative potential fully, see Table 1. The efficiency of the parabolic dish is independent from $r_{c,DP}$ as shown in Section 3.1.5), whereas the efficiency of the receiver increases with pressure ratio slightly because of the higher air density. Shaft speed increases with pressure ratio according to the Euler equation because more work is needed whereas the aperture areas of dish and receiver increase with $r_{c,DP}$ due to the higher heat input that comes about because of the decreasing inlet temperature to the receiver (lower turbine exhaust temperature.

In the light of the information in Fig. 13 and in order to maintain a feasible shaft speed in the order of 130krpm, a pressure ratio lower of 3 is selected for the design case. Even if this is lower than the optimum value, the impact on the design solar-to-electric efficiency is lower than 1% whilst still bringing about considerable reductions in shaft speed, dish area and net electric output (smaller system).

Table 3 summarizes the dependent variables considered in the design process whose values correspond to the optimum pressure ratio of both systems. The *base-case* system produces more then 7 kW_e with an aperture area of 50 m^2 while the *advanced* system generates 9 kW_e approximately (about 25%

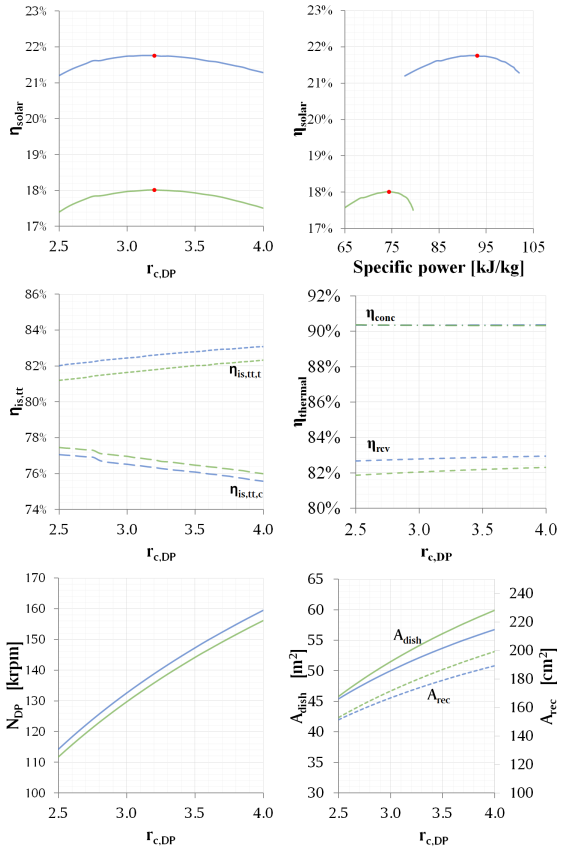

Figure 13: Solar-to-electric efficiency vs. pressure ratio and specific power (above), turbomachinery total-to-total efficiencies vs. pressure ratio (center) and shaft speed and dish/receiver aperture areas vs. pressure ratio (below). *Base-case* and *advanced* systems shown in green and blue respectively.

more) with a 3% larger aperture area only. This power gain is mainly due to the higher TIT and $\epsilon_{reg,DP}$ which raise the mean temperature of heat addition to the working cycle, transformations $3' - 4'$ and $3'' - 4''$ in Fig. 3. On the other hand, the aperture area must be increased by 12% in the *advanced* system as compared to the *base-case* if the same lower value of $\epsilon_{reg,DP}$ (85%) is considered.

4.2. Results of the annual simulations

In order to evaluate and analyze the results of the off-design model, the following three additional performance metrics are introduced:

Base-case system			
$P_{el,DP}$	7.19 kW_e	$\eta_{is,t,DP}$	82.44 %
A_{dish} (d_{dish})	50.0 m^2 (8.0 m)	$\eta_{is,c,DP}$	76.52 %
A_{SR} (d_{SR})	167 cm^2 (14.6 cm)	$\eta_{dish,DP}$	90.35 %
$A_{ex,rec}$	5570 m^2	$\eta_{rec,DP}$	82.79 %
$NTU_{rec,DP}$	5.45	$\eta_{cycle,DP}$	24.03 %
N_{DP}	129690 rpm	$\eta_{solar,DP}$	17.97 %
$\hat{P}_{sol,DP}$	0.144 kW_e/m^2	$\hat{P}_{el,DP}$	71.9 kW_e/kg
Advanced system			
$P_{el,DP}$	8.96 kW_e	$\eta_{is,t,DP}$	81.64 %
A_{dish} (d_{dish})	51.5 m^2 (8.1 m)	$\eta_{is,c,DP}$	76.97 %
A_{SR} (d_{SR})	171 cm^2 (14.8 cm)	$\eta_{dish,DP}$	90.34 %
$A_{ex,rec}$	8757 m^2	$\eta_{rec,DP}$	82.04 %
$NTU_{rec,DP}$	8.58	$\eta_{cycle,DP}$	29.34 %
N_{DP}	132540 rpm	$\eta_{solar,DP}$	21.74 %
$\hat{P}_{sol,DP}$	0.174 kW_e/m^2	$\hat{P}_{el,DP}$	89.6 kW_e/kg

Table 3: Main design specifications of the *base-case* and *advanced* systems and their components at 800 W/m^2 and the optimum $r_{c,DP}$.

- The mean annual conversion efficiency (η_{annual}, Eq. (35)) is the ratio from the annual yield (net) ($E_{el,net}$) to the available solar energy input (E_{sol}) over the year. The latter may differ from the solar energy actually harvested by the system (Q_{sol}) due to the outage (system not working) of the system for $DNI < DNI_{cut-in}$ and $DNI > DNI_{cut-off}$, Fig. 9.

- The capacity factor of the system ($f_{capacity}$, Eq. (36)) is the ratio from the annual yield ($E_{el,net}$) to the electric energy that would be produced if the system worked at the nominal output ($P_{el,DP}$) throughout the year (8760 hours).

- The dumped solar energy factor (f_{dumped}, Eq. (37), is the ratio from the solar energy that is available but not harvested by the system ($E_{sol} - Q_{sol}$) to the available solar energy input (E_{sol}). This metric is used to quantify the fraction of available solar eneryg cannot be harvested because the system is already running at full capacity.

$$\eta_{annual} = \frac{E_{el,net}}{Q_{sol}} \tag{35}$$

$$f_{capacity} = \frac{E_{el,net}}{P_{el,DP} \cdot 8760} \tag{36}$$

$$f_{dumped} = 1 - \frac{E_{sol} - Q_{sol}}{E_{sol}} \tag{37}$$

Figure 14 shows the performance maps obtained for the *base-case* (blue) and *advanced* (red) systems. The inability to absorb a very high radiation becomes evident in the upper charts for increasing DNI and translates into a drastic drop in efficiency (bottom charts) due to a large fraction of the available solar energy not being converted into useful work.

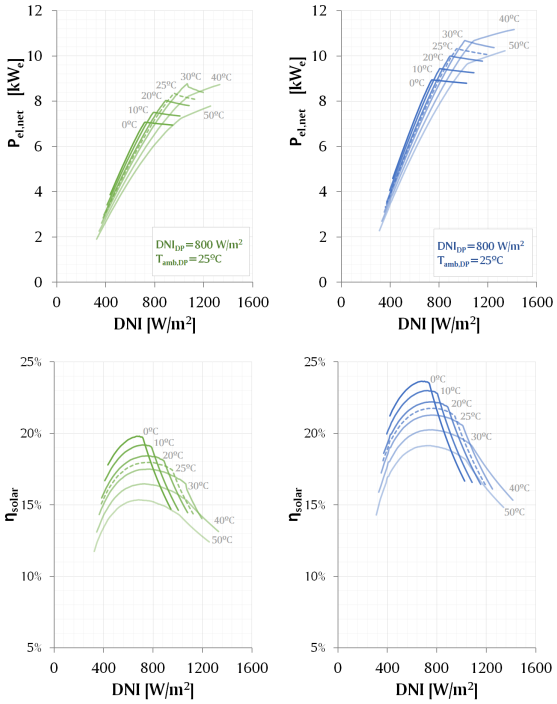

Figure 14: Performance maps of the *base-case* (left) and *advanced* (right) systems: net power output vs. DNI (above) and solar-to-electric efficiency vs. DNI (below)

Regardless of the behavior shown in Fig. 14, the maps are used to perform annual simulations in three different locations: Beijing (China), Seville (Spain) and San Diego (USA). According to the results shown in Table 4, the highest yield is obtained in San Diego where the *base-case* system achieves 15.87% annual conversion efficiency and 24.77% capacity factor, with just 10.69% of the available solar energy being dumped out of the system. Seville shows a similar performance but, in contrast, the efficiency in Beijing is just 11.13% and the capacity factor is 10.51%, mainly due to the high amount of dumped solar energy (more than 37%). It must be noted that the high f_{dumped} in this location is not due to frequent overflows of solar energy

($DNI > DNI_{cut-off}$) but to long periods of time with DNI lower than the cut-in value ($DNI > DNI_{cut-off}$). Finally, when the *advanced* systems are considered, these yied similar performances in terms of dumped solar energy and capacity factors whereas the annual efficiency is around 2.7-3.5 percentage points higher in all locations.

Base-case system			
Locations	Beijing	Seville	San Diego
$DNI_{DP}[W/m^2]$	800	800	800
$E_{sol}[kWh]$	59494	88676	98304
$Q_{sol}[kWh]$	37223	76273	87797
$E_{el,net}[kWh]$	6622	13384	15605
η_{annual}	11.13%	15.09%	15.87%
f_{dumped}	37.43%	13.99%	10.69%
$f_{capacity}$	10.51%	21.24%	24.77%
Advanced system			
Locations	Beijing	Seville	San Diego
$DNI_{DP}[W/m^2]$	800	800	800
$E_{sol}[kWh]$	61257	91304	101217
$Q_{sol}[kWh]$	39424	79669	91087
$E_{el,net}[kWh]$	8463	16938	19581
η_{annual}	13.82%	18.55%	19.35%
f_{dumped}	35.64%	12.74%	10.01%
$f_{capacity}$	10.78%	21.58%	24.95%

Table 4: Performance of the *base-case* and *advanced* systems designed for 800 W/m^2 in a Typical Meteorological Year (TMY).

4.3. Sensitivity analysis. Impact of design DNI

Sections 4.1 and 4.2 have shown that largely different performances can be obtained when the same system is operated under dissimilar boundary conditions. For this reason, a sensitivity analysis is now performed in order to assess to what extent the location impacts the optimum design DNI; i.e., DNI_{DP} that yields highest annual efficiency (η_{annual}, Eq. (35). This metric depends on the hourly distribution of DNI and on the performance maps of the system.

The sensitivity analysis is performed following the procedure shown in Figure 15. Mass flow rate and turbine inlet temperature are set to their rated values (0.1 kg/s and 800/900 °C for the *base-case*/*advanced* systems, respectively) and the value of DNI at the design point (external loop) is changed in the range of interest (400-1000 W/m^2). This means that the micro turbine design remains unaltered with respect to the original design for DNI_{DP}=800 W/m^2 whereas the solar subsystem (parabolic dish and volumetric receiver) has to be re-sized according to the new value of DNI_{DP}.

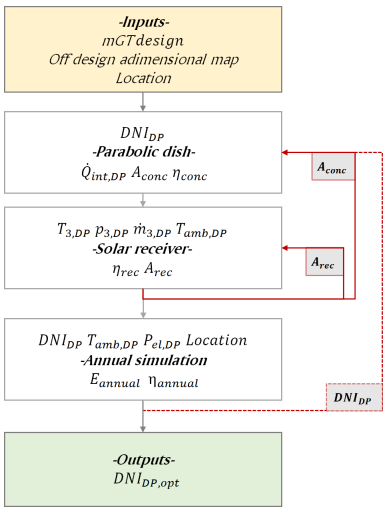

Figure 15: DNI sensitivity analysis flowchart.

The calculations for each DNI_{DP} are based on non-dimensional performance maps of the system, obtained from those shown in Section 3.2 for the reference case at 800 W/m^2. These maps shown in Fig. 14 are then dimensionalized again by merely multiplying the horizontal scale by the corresponding value of DNI_{DP}. The procedure is not utterly accurate but the error incurred does not bring about significant deviations in terms of annual system performance because the efficiency of the parabolic dish is rather independent from its size within reasonable limits (see Eqs. (16) to (20)), while the efficiency of the receiver is only slightly affected by DNI for given TIT and T_{amb}. Moreover, the performance maps obtained with the non-dimensional approach and those built using the complete off-design procedure in Section 3.2 are shown in solid blue and dotted white lines in Fig. 16, confirming that there is very good agreement in all cases.

The resulting variations of η_{annual}, $f_{capacity}$ and f_{dumped} of the *base case* and *advanced* systems are shown in Fig. 17. The lower optimal DNI_{DP} is found for Beijing (660 W/m^2 for the *base-case* system and 610 W/m^2 for the *advanced* system) whilst the highest $DNI_{DP,opt}$ corresponds to San Diego (815 W/m^2 for both systems), Seville laying in between (715 W/m^2 and 705 W/m^2). The following features are worth noting:

- There exists a visible optimum value of DNI_{DP} for each location. Designing the system for a value different to this one, for instance if a

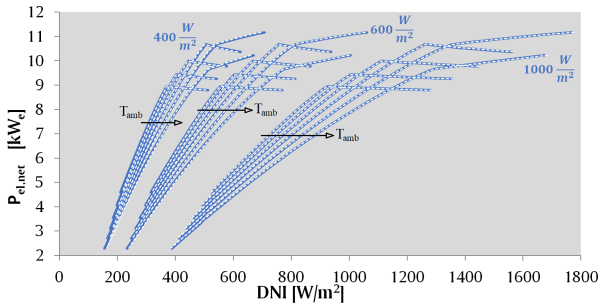

Figure 16: Validation of the performance maps used in the DNI sensitivity analysis: maps calculated with the complete off-design procedure (dotted white) and non-dimensional maps (solid blue).

universal DNI_{DP} were used, would inevitably bring about a drastic performance drop (η_{annual}).

- The previous statement is stronger in locations with low DNI whereas small changes in DNI_{DP} around the optimum value do not imply a large decrease in η_{annual} if the available DNI is high.

- Interestingly, the values of DNI_{DP} that optimize the capacity factor or dumped solar energy factor in a specific location are generally lower than the value $DNI_{DP,opt}$ that yields highest annual conversion efficiency.

The rated specifications of the dish-mGT systems designed for the optimum DNI_{DP} are summarized in Table 5 while Table 6 shows the corresponding annual performances. It is easily observed that the required dish and receiver aperture areas are higher than those calculated for 800 W/m^2 which brings about a slightly lower nominal solar-to-electric efficiency due to the higher thermal losses (which are proportional to the receiver area). Nevertheless, in spite of this, there is a significant gain in the annual yield in Beijing and Seville with respect to the reference case with DNI_{DP}=800 W/m^2 (34-48% and 14-16% respectively) while the electricity production in San Diego remains almost constant. The latter insensitivity is due to the optimum DNI_{DP} in San Diego being close to the reference value of 800 W/m^2. These results underline the importance of a proper selection of DNI_{DP} for each location which turns this parameter into a project-specific design variable. A further step, which is beyond the scope of this paper, would be to

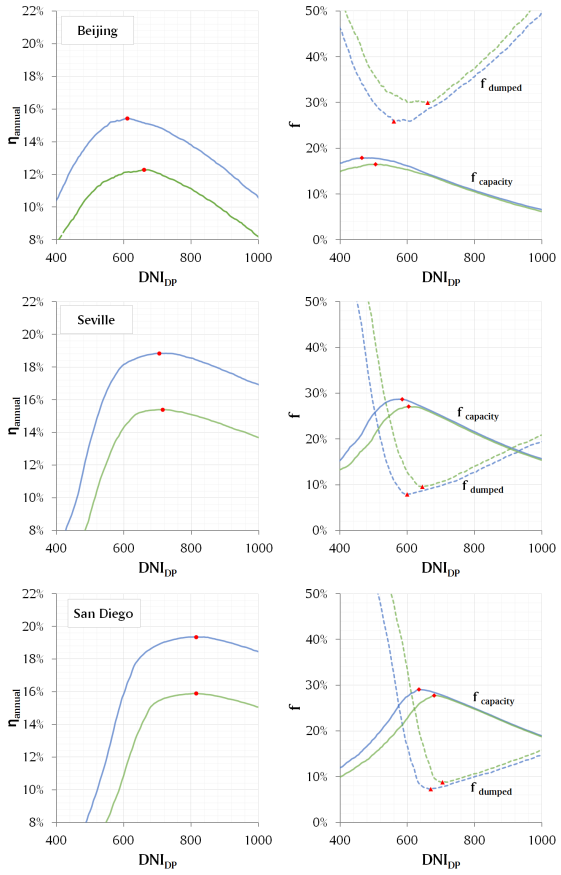

Figure 17: Mean annual solar-to-electric conversion efficiency vs DNI_{DP} for the three selected locations: *base-case* (above) and *advanced* (below) systems.

search for the DNI_{DP} that minimizes the levelized cost of electricity (LCoE) over the expected lifetime of the project. To this end, an optimization procedure would be necessary to balance the impact of dish size, main economic driver of the system that is directly proportional to the cost and inversely proportional to the amount of electricity produced.

	Base-case system		
	Beijing	Seville	San Diego
DNI_{DP}	660	715	815
A_{dish}	60.9 m^2	56.1 m^2	49.1 m^2
d_{dish}	8.8 m	8.5 m	7.9 m
A_{SR}	203 cm^2	187 cm^2	164 cm^2
d_{SR}	16.1 cm	15.4 cm	14.4 cm
$\eta_{dish,DP}$	90.34%	90.34%	90.35%
$\eta_{rec,DP}$	82.48%	82.62%	82.82%
$\eta_{solar,DP}$	17.90%	17.93%	17.98%
	Advanced system		
	Beijing	Seville	San Diego
DNI_{DP}	610	705	815
A_{dish}	68.1 m^2	58.7 m^2	50.5 m^2
d_{dish}	9.3 m	8.6 m	8.0 m
A_{SR}	227 cm^2	195 cm^2	168 cm^2
d_{SR}	17.0 cm	15.8 cm	14.6 cm
$\eta_{dish,DP}$	90.33%	90.33%	90.34%
$\eta_{rec,DP}$	81.33%	81.73%	82.08%
$\eta_{solar,DP}$	21.55%	21.66%	21.76%

Table 5: Main design features of the *base-case* and *advanced* systems at the optimum DNI_{DP}

.

In order to clarify the previous discussion further, Fig. 18 shows the difference in power production between the *base-case* (above) and *advanced* (below) systems sized for 800 W/m^2 and the optimum DNI (Table 6); these results correspond to the week 18-25 June of the TMY in Seville. It becomes evident that the dashed lines representing the optimized system are always above the solid lines representing the system designed for 800 W/m^2. This increases the capacity factor of the system and is expected to consequently reduce the levelized cost of electricity.

5. Validation of numerical models

The numerical models of the complet dish-mGT system cannot be validated directly since there are no systems of the same size available in the market nor in literature. Nevertheless, the model is expected to provide

Base-case system			
Locations	Beijing	Seville	San Diego
DNI_{DP} [W/m^2]	660	715	815
E_{sol} [kWh]	72396	99435	96463
Q_{sol} [kWh]	50719	88640	85939
$E_{el,net}$ [kWh]	8895	15320	15334
η_{annual}	12.29%	15.41%	15.90%
f_{dumped}	29.94%	10.86%	10.91%
$f_{capacity}$	14.12%	24.32%	24.34%
Advanced system			
Locations	Beijing	Seville	San Diego
DNI_{DP} [W/m^2]	610	705	815
E_{sol} [kWh]	81048	104002	99303
Q_{sol} [kWh]	60026	93666	89076
$E_{el,net}$ [kWh]	12508	19595	19222
η_{annual}	15.43%	18.84%	19.36%
f_{dumped}	25.94%	9.94%	10.30%
$f_{capacity}$	15.94%	24.97%	24.49%

Table 6: Performance of the *base-case* and *advanced* systems designed for $DNI_{DP,opt}$ and a Typical Meteorological Year (TMY).

results that are close to reality because the individual models of the constituents were previously validated against theoretical or experimental data. In particular:

- The models used to produce the performance maps of the compressor and turbine are well known and have been validated against a very large set of experimental data taken from real applications [48, 49].
- Both the design and off-design models of the solar components (parabolic dish and volumetric receiver) have been validated against data obtained at the test rig in the Royal Institute of Technology in Stockholm (KTH) [18, 19].
- The off-design model of the electric generator is derived from experimental data obtained by ENEA directly [8].
- The properties of dry air with real gas behavior are computed with Coolprop® whose accuracy is widely acknowledged within the industrial and scientific communities [45].

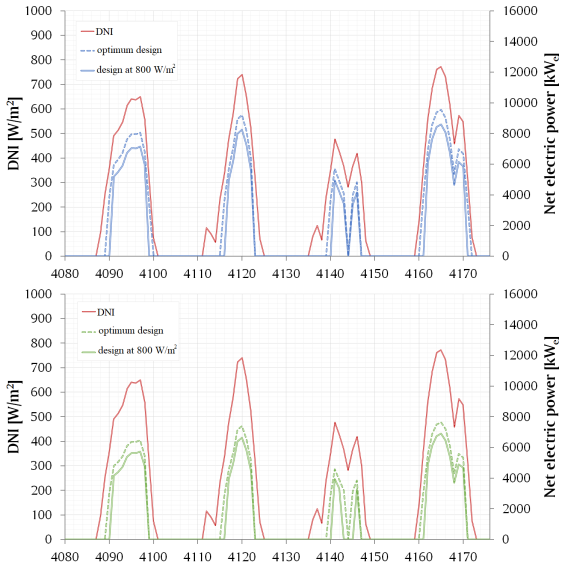

Figure 18: Comparison between the power generations of the base-case (below) and advanced (above) systems sized for 800 $\frac{W}{m^2}$ (green and blue solid lines) and for the optimum DNI (green and blue dotted lines) in the days 19-22 June of the TMY.

6. Conclusions

A novel integrated procedure to design a solar dish-mGT system and evaluate its performance has been presented with a specific focus on the geometry and specifications of the components that yield the best performance. An innovative control strategy has also been proposed with the objective to avoid overheating and overloading of the system under any operating conditions (DNI and ambient temperature).

The design model was run for two different sets of turbine inlet temperatures and recuperator effectiveness (TIT and $\epsilon_{reg,DP}$): 800°C-85% for the *base-case* and 900°C-90% dor the *advanced* system. Different systems are designed for each case (geometry and efficiency of components, thermodynamic states of the working cycle, turbomachinery performance maps) which yield different off-design performance maps linking the net power output of the total system to the boundary conditions (ambient temperature and DNI).

With this information, annual simulations were performed for three selected locations (Beijing, Seville and San Diego) based on performance maps adapted to their particular DNI. The results show that there is a large potential for performance gain when the system is designed with a project-

specific DNI_{DP} in lieu of a standard DNI_{DP} (with a reference value of 800 W/m^2). For the cases considered, the mean annual conversion efficiency of the *base-case* and *advanced* systems can potentially increase by 11%-16% and 14%-19% respectively.

Finally, with regards to the annual production of electricity, the figures in the previous paragraph translate into a very large increase which can be as high as almost 50% for the case of Beijing. These results emphasize the importance of selecting the design specifications in accordance with the local meteorological conditions along a typical year in order to maximize the production of electricity and in turn minimize costs.

7. Acknowledgements

This paper has party been funded by the European Commission under Grant Agreement No. 308952 of the 7^{th} Framework Programme: *Optimised Microturbine SOlar Power system - OMSoP*. The authors are also grateful to the OMSoP consortium mebers for sharing technical information used to fine tune the model of performance presented herein.

8. References

[1] R. Buck, T. BraÌĺuning, T. Denk, M. PfaÌĺnder, P. SchwarzboÌĺzl, F. Tellez, Solar-hybrid gas turbine-based power tower systems (refos), Journal of Solar Energy Engineering 124 (1) (2002) 2–9.

[2] P. Schwarzbözl, R. Buck, C. Sugarmen, A. Ring, M. J. M. Crespo, P. Altwegg, J. Enrile, Solar gas turbine systems: design, cost and perspectives, Solar Energy 80 (10) (2006) 1231–1240.

[3] C. Sugarmen, F. Tellez, R. Buck, J. Medina, P. Altwegg, A. Ring, M. Romero, P. Heller, P. Schwarzbözl, Solgate: Solar hybrid gas turbine electric power system, Final Report.

[4] M. Quero, R. Korzynietz, M. Ebert, A. Jiménez, A. Del Río, J. Brioso, Solugas–operation experience of the first solar hybrid gas turbine system at mw scale, Energy Procedia 49 (2014) 1820–1830.

[5] R. Korzynietz, J. Brioso, A. del Río, M. Quero, M. Gallas, R. Uhlig, M. Ebert, R. Buck, D. Teraji, Solugas–comprehensive analysis of the solar hybrid brayton plant, Solar Energy 135 (2016) 578–589.

[6] ETN, Omsop project (2013).
URL https://omsop.serverdata.net/

[7] A. Giovannelli, State of the art on small-scale concentrated solar power plants, Energy Procedia 82 (2015) 607–614.

[8] E. OMSOP, Project, deliverable d3.4-report on state-of-the-art dish-engine applications, july 2013.

[9] M. Lanchi, M. Montecchi, T. Crescenzi, D. Mele, A. Miliozzi, V. Russo, D. Mazzei, M. Misceo, M. Falchetta, R. Mancini, Investigation into the Coupling of Micro Gas Turbines with CSP Technology: OMSoP Project, Energy Procedia 69 (2015) 1317 – 1326.

[10] G. Cerri, I. Bernardini, A. Giovannelli, L. Chennaoui, A gas turbine high efficiency cycle fed by concentrated solar power.

[11] D. SÃąnchez, A. Bortkiewicz, J. M. RodrÃŋguez, G. S. MartÃŋnez, G. Gavagnin, T. SÃąnchez, A methodology to identify potential markets for small-scale solar thermal power generators, Applied Energy 169 (2016) 287 – 300.

[12] G. Gavagnin, D. Sánchez, G. S. Martínez, J. M. Rodríguez, A. Muñoz, Cost analysis of solar thermal power generators based on parabolic dish and micro gas turbine: Manufacturing, transportation and installation, Applied Energy 194 (2017) 108–122.

[13] G. Gavagnin, D. Sánchez, J. Rodríguez, A. Muñoz, G. Martínez, Economic Competitiveness of Dish-mGT Solar Power Generators (GT2017-64351), in: ASME-IGTI (Ed.), ASME 2017 Turbo Expo: Turbine Technical Conference and Exposition, Charlotte, NC, 2017.

[14] W. Visser, S. Shakariyants, M. Oostveen, Development of a 3 kW Microturbine for CHP applications, Journal of Engineering for Gas Turbines and Power 133 (2011) 042301.

[15] T. Hynes, The most eficient small gas turbines in the world, in: Ecosummit, Berlin, 2017.

[16] C. Soares, Microturbines: applications for distributed energy systems, Butterworth-Heinemann, 2011.

[17] K. Lovegrove, W. Stein, Concentrating solar power technology: principles, developments and applications, Elsevier, 2012.

[18] L. Aichmayer, J. Spelling, W. Wang, B. Laumert, Design and analysis of a solar receiver for micro gas turbine based solar dish systems, in: International SolarPACES Conference 2012. Marrakesh, Morocco. September 11-14, 2012.

[19] L. Aichmayer, J. Spelling, B. Laumert, Preliminary design and analysis of a novel solar receiver for a micro gas-turbine based solar dish system, Solar Energy 114 (2015) 378–396.

[20] W. Wang, H. Xu, B. Laumert, T. Strand, An inverse design method for a cavity receiver used in solar dish brayton system, Solar Energy 110 (2014) 745–755.

[21] L. Aichmayer, J. Spelling, B. Laumert, T. Fransson, Micro gas-turbine design for small-scale hybrid solar power plants, Journal of engineering for gas turbines and power 135 (11) (2013) 113001.

[22] L. Aichmayer, J. Spelling, B. Laumert, Small scale hybrid solar power plants for polygeneration in rural areas, Energy Procedia 57 (2014) 1536–1545.

[23] L. Aichmayer, J. Spelling, B. Laumert, Thermoeconomic analysis of a solar dish micro gas-turbine combined-cycle power plant, Energy Procedia 69 (2015) 1089–1099.

[24] W. Wang, G. Ragnolo, L. Aichmayer, T. Strand, B. Laumert, Integrated design of a hybrid gas turbine-receiver unit for a solar dish system, Energy Procedia 69 (2015) 583–592.

[25] J. Kesseli, A. Wells, Cost competitive 30 kWe gas turbine/generator demonstration for cogeneration or solar-electric applications, in: IEEE (Ed.), 24^{th} International Energy Conversion Engineering Conference, 1989, pp. 1903 – 1908.

[26] B. Dickey, Test Results From a Concentrated Solar Microturbine Brayton Cycle Integration GT2011-45918, in: ASME-IGTI (Ed.), ASME 2011 Turbo Expo: Turbine Technical Conference and Exposition, 2011, pp. 2013–1036.

[27] W. G. Le Roux, J. P. Meyer, Modeling the small-scale dish-mounted solar thermal brayton cycle, in: SOLARPACES 2015: International Conference on Concentrating Solar Power and Chemical Energy Systems, Vol. 1734, AIP Publishing, 2016, p. 060002.

[28] S. Semprini, D. Sánchez, A. De Pascale, Performance analysis of a micro gas turbine and solar dish integrated system under different solar-only and hybrid operating conditions, Solar Energy 132 (2016) 279–293.

[29] L. D. Jaffe, A review of test results on solar thermal power modules with dish-mounted stirling and brayton cycle engines, Journal of solar energy engineering 110 (4) (1988) 268–274.

[30] W. B. Stine, R. B. Diver, A compendium of solar dish/stirling technology, Tech. rep., DTIC Document (1994).

[31] J. Coventry, C. Andraka, Dish systems for {CSP}, Solar Energy.

[32] R. L. Johnson, Subatmospheric brayton-cycle engine program review, Tech. rep., AiResearch Mfg. Co., Torrance, CA (USA) (1984).

[33] E. staff of Garrett Turbine Engine Componay, Brayton cycle solarized advanced gas turbine: Final report, Tech. rep., NASA (1986).

[34] L. Amsbeck, T. Denk, M. Ebert, C. Gertig, P. Heller, P. Herrman, J. Jedamski, J. John, P. Tobias, J. Rehn, Test of a solar-hybrid microturbine system and evaluation of storage deployment.

[35] B. Dickey, Test results from a concentrated solar microturbine brayton cycle integration, in: ASME 2011 Turbo Expo: Turbine Technical Conference and Exposition, American Society of Mechanical Engineers, 2011, pp. 1031–1036.

[36] J. Kesseli, Brayton power conversion system, Tech. rep., Brayton Energy (2012).

[37] P. Heller, R. Buck, T. Biehler, Development of a Volumetric Receiver for a Dish-Brayton System, in: ASME (Ed.), ASME Joint Solar Engineering Conference, 1996.

[38] R. Buck, P. Heller, H. Koch, Receiver development for a Dish-Brayton system, in: ASME (Ed.), ASME International Solar Energy Conference, San Antonio, TX, 1996.

[39] C. Rodgers, C. F. McDonald, Small recuperated gas turbine APU concept to abate concern about emissions, high fuel cost, and noise, in: ASME Turbo Expo 2007: Power for Land, Sea, and Air, Montreal, Canada, 2007, pp. 383–391.

[40] C. Rodgers, Thermo-Economics of a small 50 kW Turbogenerator, in: ASME 1997 International Gas Turbine and Aeroengine Congress and Exhibition, American Society of Mechanical Engineers, Orlando, FL, 1997.

[41] C. Rodgers, Turbochargers to small gas turbines?, in: ASME 1997 International Gas Turbine and Aeroengine Congress and Exhibition, Orlando, FL, 1997.

[42] P. F. Myers, Economics and Design Approaches for Small Commercial Turbogenerators, in: ASME 1997 International Gas Turbine and Aeroengine Congress and Exhibition, Orlando, FL, 1997.

[43] C. F. McDonald, C. Rodgers, The ubiquitous personal turbine - A power vision for the 21st century, in: ASME Turbo Expo 2001: Power for Land, Sea, and Air, New Orleans, LO, 2001.

[44] D. Gallup, J. Kesseli, A solarized Brayton engine based on turbo-charger technology and the DLR receiver, in: Intersociety Energy Conversion Engineering Conference, Vol. 4, American Nuclear Society, 1994, pp. 1719–1719.

[45] I. H. Bell, J. Wronski, S. Quoilin, V. Lemort, Pure and pseudo-pure fluid thermophysical property evaluation and the open-source thermophysical property library coolprop, Industrial & Engineering Chemistry Research 53 (6) (2014) 2498–2508. arXiv:http://pubs.acs.org/doi/pdf/10.1021/ie4033999, doi:10.1021/ie4033999.
URL `http://pubs.acs.org/doi/abs/10.1021/ie4033999`

[46] MATLAB, version 7.10.0 (R2010a), The MathWorks Inc., Natick, Massachusetts, 2010.

[47] M. J. Moran, H. N. Shapiro, D. D. Boettner, M. B. Bailey, Fundamentals of engineering thermodynamics, John Wiley & Sons, 2010.

[48] R. H. Aungier, Centrifugal compressors (2000).

[49] R. H. Aungier, Turbine aerodynamics, American Society of Mechanical Engineers Press, New York.

[50] B. M. Gallo, M. S. El-Genk, J.-M. Tournier, M. S. El-Genk, Compressor and turbine models of brayton units for space nuclear power systems, in: AIP Conference Proceedings, Vol. 880, AIP, 2007, pp. 472–482.

[51] C. Rodgers, Microturbine rotational speed selection, in: ASME Turbo Expo 2013: Turbine Technical Conference and Exposition, American Society of Mechanical Engineers, 2013, pp. V05AT23A005–V05AT23A005.

[52] O. Balje, A study on design criteria and matching of turbomachines: Part aâĂŤsimilarity relations and design criteria of turbines, Journal of Engineering for Power 84 (1) (1962) 83–102.

[53] O. Balje, A study on design criteria and matching of turbomachines: Part bâĂŤcompressor and pump performance and matching of turbocomponents, Journal of Engineering for Power 84 (1) (1962) 103–114.

[54] O. Balje, A study on reynolds number effects in turbomachines, Journal of Engineering for Power 86 (3) (1964) 227–235.

[55] A. J. Head, W. Visser, Scaling 3-36kw microturbines, in: ASME Turbo Expo 2012: Turbine Technical Conference and Exposition, American Society of Mechanical Engineers, 2012, pp. 609–617.

[56] C. Rodgers, A cycle analysis technique for small gas turbines, Solar Division (1969) 37–49.

[57] J. Nikuradse, Laws of flow in rough pipes, National Advisory Committee for Aeronautics Washington, 1950.

[58] J. E. Hesselgreaves, R. Law, D. Reay, Compact heat exchangers: selection, design and operation, Butterworth-Heinemann, 2016.

[59] R. Shah, Compact heat exchangers for microturbines.

[60] C. F. McDonald, Low-cost compact primary surface recuperator concept for microturbines, Applied Thermal Engineering 20 (5) (2000) 471–497.

[61] C. F. McDonald, Recuperator considerations for future higher efficiency microturbines, Applied Thermal Engineering 23 (12) (2003) 1463–1487.

[62] A. Traverso, A. F. Massardo, Optimal design of compact recuperators for microturbine application, Applied Thermal Engineering 25 (14) (2005) 2054–2071.

[63] M. Röger, C. Rickers, R. Uhlig, F. Neumann, C. Polenzky, Infrared-reflective coating on fused silica for a solar high-temperature receiver, Journal of Solar Energy Engineering 131 (2) (2009) 021004.

[64] J. R. Welty, C. E. Wicks, G. Rorrer, R. E. Wilson, Fundamentals of momentum, heat, and mass transfer, John Wiley & Sons, 2009.

[65] W. B. Stine, R. W. Harrigan, Solar energy fundamentals and design, John Wiley and Sons, Inc., New York, NY, 1985.

[66] W. B. Stine, M. Geyer, Power from the Sun, Power from the sun. net, 2001.

[67] J. A. Harris, W. S. Duff, Focal plane flux distributions produced by solar concentrating reflectors, Solar Energy 27 (5) (1981) 403–411.

[68] M. Ghavami, J. Alzaili, I. Sayma, A., A comparative study of the control strategies for pure concentrated solar power micro gas turbines (GT2017-63987), in: ASME-IGTI (Ed.), ASME 2017 Turbo Expo: Turbine Technical Conference and Exposition, 2017.

[69] J. Noall, M. Forsha, Off-design turbomachinery performance mapping, Barber Nichols Inc., Internal Program Report.

[70] A. J. Glassman, Turbine design and application. nasa sp-290, NASA Special Publication 290.